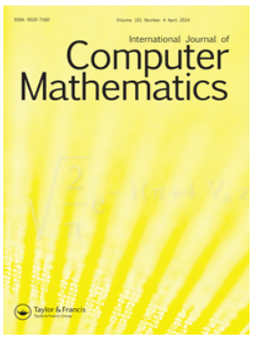

International Journal of Computer Mathematics

ISSN: (Print) (Online) Journal homepage: www.tandfonline.com/journals/gcom20

Stabilized equal lower-order finite element methods for simulating Brinkman equations in porous media

Hsueh-Chen Lee & Hyesuk Lee

To cite this article: Hsueh-Chen Lee & Hyesuk Lee (19 Apr 2024): Stabilized equal lower-order finite element methods for simulating Brinkman equations in porous media, International Journal of Computer Mathematics, DOI: 10.1080/00207160.2024.2343102

To link to this article: https://doi.org/10.1080/00207160.2024.2343102

Published online: 19 Apr 2024.

INTERNATIONAL JOURNAL OF COMPUTER MATHEMATICS
https://doi.org/10.1080/00207160.2024.2343102

Taylor & Francis
Taylor & Francis Group

RESEARCH ARTICLE

Stabilized equal lower-order finite element methods for simulating Brinkman equations in porous media

Hsueh-Chen Lee[a] and Hyesuk Lee[b]

[a]Center for General Education, Wenzao Ursuline University of Languages, Kaohsiung, Taiwan; [b]School of Mathematical and Statistical Sciences, Clemson University, Clemson, SC, USA

ABSTRACT

This paper demonstrates the mixed formulation of the Brinkman problem using linear equal-order finite element methods in porous media modelling. We introduce Galerkin least-squares (GLS) and least-squares (LS) finite element methods to address the incompatibility of finite element spaces, treating velocity, pressure, and vorticity as independent variables. Theoretical analysis examines coercivity and continuity, providing error estimates. Demonstrating resilience in theoretical findings, these methods achieve optimal convergence rates in the L^2 norm by incorporating stabilization terms with low-order basis functions. Numerical experiments validate theoretical predictions, showing the effectiveness of the GLS method and addressing finite element space incompatibility. Additionally, the GLS method exhibits promising capabilities in handling the Brinkman equation at low permeability compared to the LS method. The study reveals an increase in the average pressure difference in the Brinkman problem compared to the Stokes equations as the inlet velocity rises, providing insights into the behaviour of Brinkman equations.

ARTICLE HISTORY
Received 6 December 2023
Revised 4 March 2024
Accepted 8 April 2024

KEYWORDS
Galerkin least-squares; least-squares; equal-order finite elements; stabilization finite element method; pore-scale flow

AMS SUBJECT CLASSIFICATIONS
76-10; 76M10; 65N30

1. Introduction

Understanding the intricate dynamics of fluid movement through tiny rock pores is paramount in challenging underground reservoirs with limited natural fluid flow. The behaviour of fluids within these porous structures not only impacts resource extraction but also holds significant implications for environmental and geological considerations [26]. This paper addresses the complex challenge of characterizing fluid flow at the microscopic level within porous rock formations. The specific problem we aim to tackle is understanding how fluids traverse these tortuous pathways in cases where natural fluid flow is limited. This question lies at the heart of efficient underground reservoir management, influencing a wide range of industries, from energy production to environmental conservation.

The Brinkman equations have proven indispensable in describing flow in porous media. Prior studies, such as those by Hwang and Advani, Iliev et al., and Ingeram [13–15], have applied the Brinkman equations to perform numerical simulations and explore permeability in porous media, underlining the mathematical properties and stability of the equations [15]. Recent advances in the Brinkman problem indicated that the Galerkin finite element methods, including hybridizable discontinuous Galerkin method, mixed finite element and stabilized techniques [3,21,23,27,29] have improved the accuracy and stability of solutions.

CONTACT Hsueh-Chen Lee 87013@mail.wzu.edu.tw Center for General Education, Wenzao Ursuline University of Languages, 900 Mintsu 1st Road Kaohsiung, Taiwan

However, the need for velocity-pressure interpolations that satisfy inf-sup conditions poses challenges [3]. Recent investigations [11,20] suggest that finite element methods employing equal lower-order elements yield more satisfactory results and incur lower computational costs than those utilizing higher-order elements. Enhancing accuracy with lower-order elements often entails mesh refinement [19]. This strategy is simpler to implement and demands fewer computational resources, rendering it suitable for specific applications, particularly when computational efficiency is paramount. To address space incompatibility, some studies [4,7,9,11,25,28] introduce the linear order finite element methods based on the weak Galerkin and the Galerkin least-square (GLS) finite element methods, interpolating stabilization terms in the governing equations to enhance the stability and accuracy of finite element solutions. Additionally, the least-squares (LS) finite element method offers a viable alternative that does not require the inf-sup condition [6,17–20].

This paper employs a mixed formulation of the Brinkman equations to model pore-scale flow through rock pores, introducing flow vorticity as an additional unknown. While incorporating vorticity as an independent unknown aligns with established techniques in the Brinkman problem [1,27], our approach distinguishes itself from other velocity-pressure-vorticity formulations by incorporating the rate of deformation tensor to ensure stability. The use of the rate of deformation tensor for stability is a common practice in viscoelastic fluid problems involving velocity, pressure, and stress fields [4,10,16]. We employ lower equal-order finite element methods, including mixed finite element and stabilized techniques, specifically three types of the GLS methods and the LS method for the velocity-pressure-vorticity Brinkman equations. These approaches consider diffusion stabilization terms, and our results demonstrate their ability to achieve optimal convergence rates in the L^2 norm, even when using low-order basis functions. We also address the effect of the diffusion stabilization term. Furthermore, we extend the application of these methods to simulate creeping flow in porous media, specifically for a pore-scale flow problem. The results align with previous research, validating the efficacy of our approach. However, we have observed that as the inlet velocity increases, there is a significant amplification in the average pressure difference compared to solutions governed by the Stokes equation.

The rest of this paper is organized as follows. Section 2 presents the problem statement. Section 3 presents notation and preliminaries. Section 4 introduces the finite element approximation. Section 5 presents two numerical examples, and finally, conclusions follow in Section 6.

2. Statement of the problem

This study addresses the steady creeping flow of incompressible Newtonian fluids within the interstices of a porous medium. The specific problem at the heart of this research is to analyze and model the fluid flow behaviour in the microscopic pores of a porous medium, with a particular focus on a pore-scale geometry obtained from prior experiments [2,24,26]. Prior research conducted by Sirivithayapakorn and Keller [26] directly observed the exclusion of colloids from small-aperture areas using realistic micromodels of porous media. Auset and Keller [2] investigated the impact of particle and pore sizes on colloid dispersion through water-saturated micromodels at the pore scale. Additionally, Liu et al. [24] introduced pore-scale flow simulations using the creeping flow interface and Brinkman equation interfaces based on Comsol software.

For the creeping flow in the channels, the incompressible, stationary Brinkman (Stokes-Darcy) equations [3] is used in a two-dimensional Ω with Lipschitz boundary Γ by

$$-\mu\Delta\mathbf{u} + \nabla p + \epsilon\mathbf{u} = \mathbf{f} \text{ in } \Omega, \tag{1}$$

$$\rho\nabla\cdot\mathbf{u} = 0 \text{ in } \Omega, \tag{2}$$

$$\mathbf{u} = \mathbf{0} \text{ on } \Gamma, \tag{3}$$

where $\mathbf{u} = (u, v)$ is Darcy's velocity and p is pressure. We assume that the scalar pressure p is fixed to p_0 at the point $\mathbf{x}_0$ on Γ, i.e. $p(\mathbf{x}_0) = p_0$, to ensure the uniqueness of pressure. $\mathbf{f}$ is given data and the

physical parameters are the fluid viscosity μ and $\epsilon = \mu/\kappa$ with κ is the permeability of the medium. Notably, the momentum Equation (1) is associated with high permeability κ, leading to the condition $\epsilon\mathbf{u} = 0$, which renders the effects of the porous structure negligible. This condition is analogous to the one governing the Stokes equation for creeping flows.

3. Notation and preliminaries

Let $H^s(\Omega)$, $s \geq 0$, be the Sobolev spaces with the standard associated inner products $(\cdot,\cdot)_s$ and their respective norms $\|\cdot\|_s$. For $s = 0$, $H^s(\Omega)$ coincides with $L^2(\Omega)$. To obtain a mixed formulation of the Brinkman problem (1)–(3), we exploit, the vector calculus identity

$$-\Delta\mathbf{u} = a\nabla\times(\nabla\times\mathbf{u}) - 2(1-a)\nabla\cdot D(\mathbf{u}),$$

for a divergence-free $\mathbf{u}$, where $0 < a < 1$ and $D(\mathbf{u}) := 0.5(\nabla\mathbf{u} + \nabla\mathbf{u}^T)$ is the rate of deformation tensor. Defining the vorticity variable $\omega = \nabla\times\mathbf{u}$, we have the Velocity–Pressure-Vorticity-Deformation (VPWD) formulation [1,27] of the Brinkman Equations (1)–(3),

$$a\mu\nabla\times\omega - 2\mu(1-a)\nabla\cdot D(\mathbf{u}) + \nabla p + \epsilon\mathbf{u} = \mathbf{f} \text{ in } \Omega, \tag{4}$$

$$\omega - \nabla\times\mathbf{u} = \mathbf{0} \text{ in } \Omega, \tag{5}$$

$$\rho\nabla\cdot\mathbf{u} = 0 \text{ in } \Omega, \tag{6}$$

where the vorticity ω in $\mathbb{R}^2$ is considered a scalar and the rate of deformation tensor D is included to produce a stable effect on the solution [10,16]. Here $a = 0.5$ are considered. For $a = 0$, we consider the Velocity–Pressure-Deformation (VPD) formulation of the Brinkman Equations (4)–(6) is given by

$$-2\mu\nabla\cdot D(\mathbf{u}) + \nabla p + \epsilon\mathbf{u} = \mathbf{f} \text{ in } \Omega, \tag{7}$$

$$\omega - \nabla\times\mathbf{u} = \mathbf{0} \text{ in } \Omega, \tag{8}$$

$$\rho\nabla\cdot\mathbf{u} = 0 \text{ in } \Omega, \tag{9}$$

and for $a = 1$, the Velocity–Pressure-Vorticity (VPW) formulation of the Brinkman Equations (4)–(6) is given by

$$\mu\nabla\times\omega + \nabla p + \epsilon\mathbf{u} = \mathbf{f} \text{ in } \Omega, \tag{10}$$

$$\omega - \nabla\times\mathbf{u} = \mathbf{0} \text{ in } \Omega, \tag{11}$$

$$\rho\nabla\cdot\mathbf{u} = 0 \text{ in } \Omega. \tag{12}$$

Let $H^s(\Omega)$, $s \geq 0$ be the Sobolev spaces with the standard associated inner products $(\cdot,\cdot)_s$ and their respective norms $\|\cdot\|_s$. The function spaces used in our variational formulations are defined as:

$$\boldsymbol{X} = \{\mathbf{v} \,|\, \mathbf{v} \in \mathbf{H}^1(\Omega)^2,\ \mathbf{v} = \mathbf{0} \text{ on } \partial\Omega\},$$

$$\Sigma = L^2(\Omega),$$

$$\Sigma_1 = H^1(\Omega),$$

$$Q = \left\{ q \,|\, q \in L^2(\Omega), \int_\Omega q\,\mathrm{d}x = 0 \right\},$$

$$Q_1 = Q \cap H^1(\Omega),$$

and let the product spaces $\boldsymbol{\Phi} := \boldsymbol{X}\times\Sigma\times Q$ and $\boldsymbol{\Phi}_1 := \boldsymbol{X}\times\Sigma_1\times Q_1$.

We consider the norms as

$$\|\boldsymbol{U}\|_{\boldsymbol{\Phi}}^2 = \|\omega\|_0^2 + \|p\|_0^2 + \|\mathbf{u}\|_1^2,$$

$\forall \boldsymbol{U} = (\mathbf{u}, \omega, p) \in \boldsymbol{\Phi}$.

The Galerkin weak formulation of (4)–(6) is derived for $(\mathbf{u}, p, \omega) \in \boldsymbol{\Phi}$. For the coercivity of the associated bilinear form, (5) is multiplied by $a\mu$, first. Multiplying (4) by a test function $\mathbf{v}$ and integrating by parts, we have

$$a\mu\,(\omega, \nabla \times \mathbf{v}) + 2\mu(1-a)\,(D(\mathbf{u}), D(\mathbf{v})) - (p, \nabla \cdot \mathbf{v}) + \epsilon\,(\mathbf{u}, \mathbf{v}) = (\mathbf{f}, \mathbf{v})\,.$$

The weak formulation of (4)–(6) is then to find $\boldsymbol{U} \in \boldsymbol{\Phi}$ such that

$$\mathcal{B}(\boldsymbol{U}, \boldsymbol{V}) = \mathcal{F}(\boldsymbol{V}) \quad \forall\, \boldsymbol{V} \in \boldsymbol{\Phi}, \tag{13}$$

where

$$\begin{aligned}\mathcal{B}(\boldsymbol{U}, \boldsymbol{V}) &= a\mu\,(\omega, \nabla \times \mathbf{v}) + 2\mu(1-a)\,(D(\mathbf{u}), D(\mathbf{v})) - (p, \nabla \cdot \mathbf{v}) \\ &\quad + \epsilon\,(\mathbf{u}, \mathbf{v}) + a\mu\,(\omega - \nabla \times \mathbf{u}, \sigma) + (\rho \nabla \cdot \mathbf{u}, q)\,, \qquad (14)\\ \mathcal{F}(\boldsymbol{V}) &= (\mathbf{f}, \mathbf{v})\,. \qquad (15)\end{aligned}$$

The lower bound of $\mathcal{B}(\boldsymbol{U}, \boldsymbol{U})$ is shown as

$$\mathcal{B}(\boldsymbol{U}, \boldsymbol{U}) \geq 2\mu(1-a)\|D(\mathbf{u})\|_0^2 + \epsilon\|u\|_0^2 + a\mu\|\omega\|_0^2 \geq C(\|\mathbf{u}\|_1^2 + \|\omega\|_0^2), \tag{16}$$

and the continuity of $\mathcal{B}(\cdot, \cdot)$ is also easily obtained by the Cauchy–Schwarz inequality:

$$\begin{aligned}\mathcal{B}(\boldsymbol{U}, \boldsymbol{V}) &\leq C(\|\mathbf{u}\|_1 + \|\boldsymbol{\omega}\|_0 + \|p\|_0)(\|\mathbf{v}\|_1 + \|\boldsymbol{\sigma}\|_0 + \|q\|_0) \\ &\leq C\|\boldsymbol{U}\|_{\boldsymbol{\Phi}}\|\boldsymbol{V}\|_{\boldsymbol{\Phi}}. \qquad (17)\end{aligned}$$

Next, we consider the LS functional for the VPW formulation of Brinkman Equations (10)–(12) is given by

$$L(\boldsymbol{U}; \mathbf{f}) = \|\mu \nabla \times \omega + \nabla p + \epsilon \mathbf{u} - \mathbf{f}\|_0^2 + \|\omega - \nabla \times \mathbf{u}\|_0^2 + K\,\|\rho \nabla \cdot \mathbf{u}\|_0^2\,, \tag{18}$$

for all $\boldsymbol{U} = (\mathbf{u}, \omega, p) \in \boldsymbol{\Phi}_1$. The mass conservation weight $K = 10^m$ of the divergence term, where m ranges from 0 to 10 is chosen [18]. Their results indicate that LS solutions can be improved by sufficient weighting the divergence term.

The a priori estimate was derived for the first-order Stokes system [6], (10)–(12) with $\epsilon = 0$, that is, the coercivity for the homogeneous LS functional (18):

$$\|\mu \nabla \times \omega + \nabla p\|_0^2 + \|\omega - \nabla \times \mathbf{u}\|_0^2 + \|\rho \nabla \cdot \mathbf{u}\|_0^2 \geq C(\|\omega\|_0^2 + \|p\|_0^2 + \|\mathbf{u}\|_1^2), \tag{19}$$

for constant $C > 0$ independent of $(\mathbf{u}, \omega, p) \in \boldsymbol{\Phi}_1$. Using this estimate and the inequality $\|a+b\|^2 \geq (1/2)\|a\|^2 - \|b\|^2$ and (19), we have the lower bound of $L(\boldsymbol{U}; \mathbf{0})$ as

$$\begin{aligned}L(\boldsymbol{U}; \mathbf{0}) &\geq \|\boldsymbol{\omega} - \nabla \times \mathbf{u}\|_0^2 + K\,\|\rho \nabla \cdot \mathbf{u}\|_0^2 + \frac{1}{2}\|\mu \nabla \times \boldsymbol{\omega} + \nabla p\|_0^2 - \|\epsilon \mathbf{u}\|_0^2 \\ &\geq \|\boldsymbol{\omega} - \nabla \times \mathbf{u}\|_0^2 + K\,\|\rho \nabla \cdot \mathbf{u}\|_0^2 + \frac{1}{2}\|\mu \nabla \times \boldsymbol{\omega} + \nabla p\|_0^2 - \|\epsilon \mathbf{u}\|_1^2, \\ &\geq C(\|\omega\|_0^2 + \|p\|_0^2 + \|\mathbf{u}\|_1^2) - \epsilon^2\|\mathbf{u}\|_1^2, \\ &\geq c_0\,\|\!|\boldsymbol{U}|\!\|_{\boldsymbol{\Phi}}^2\,, \qquad (20)\end{aligned}$$

for sufficiently small ϵ so that the coefficient of the last term in (20) is positive.

For the continuity of $L(\boldsymbol{U};\mathbf{0})$ follows naturally from the triangle inequality,

$$L(\boldsymbol{U};\mathbf{0}) \le c_1(\|\omega\|_1^2 + \|p\|_1^2 + \|\mathbf{u}\|_1^2). \tag{21}$$

Therefore, the LS minimization problem for the solution of system (10)–(12) is to choose $\boldsymbol{U} = (\mathbf{u}, \omega, p) \in \boldsymbol{\Phi}_1$ such that

$$L(\boldsymbol{U};\mathbf{f}) = \inf_{\boldsymbol{V}=(\mathbf{v},\sigma,q)\in\boldsymbol{\Phi}} L(\boldsymbol{V};\mathbf{f}). \tag{22}$$

4. Finite element approximation

For the finite element approximation, we assume that the domain Ω is a polygon and that mesh $\mathcal{T}_h$ is a partition of Ω into finite elements $\Omega = \bigcup_{T\in\mathcal{T}_h} T$ with mesh size $h = \max\{\mathrm{diam}(T) : T \in \mathcal{T}_h\}$. Assume that the triangulation $\mathcal{T}_h$ is regular and satisfies the inverse assumption [19]. The grid size is defined as $h = \sqrt{|\,\Omega\,|}/\sqrt{N}$, where $|\,\Omega\,|$ is the area of the domain and N is the number of elements in $\mathcal{T}_h$. Let $P_r(T)$ denote the standard space of degree r polynomials on element T. Define finite element spaces for the approximate of $\boldsymbol{U} = (\mathbf{u}, \omega, p)$:

$$\begin{aligned}
\mathbf{X}^h &= \{\mathbf{v}^h \,|\, \mathbf{v}^h \in \mathbf{X} \cap (C^0(\Omega))^2,\ \mathbf{v}^h|_T \in P_r(T)^2\ \forall T \in \mathcal{T}_h\},\\
Q^h &= \{q^h \,|\, q^h \in Q \cap C^0(\Omega),\ q^h|_T \in P_r(T)\ \forall T \in \mathcal{T}_h\},\\
Q_1^h &= \{q^h \,|\, q^h \in Q_1 \cap C^0(\Omega),\ q^h|_T \in P_r(T)\ \forall T \in \mathcal{T}_h\},\\
\Sigma^h &= \{\sigma^h \,|\, \sigma^h \in \Sigma \cap C^0(\Omega),\ \sigma^h|_T \in P_r(T)\ \forall T \in \mathcal{T}_h\},\\
\Sigma_1^h &= \{\sigma^h \,|\, \sigma^h \in \Sigma_1 \cap C^0(\Omega),\ \sigma^h|_T \in P_r(T)\ \forall T \in \mathcal{T}_h\}.
\end{aligned}$$

4.1. Stabilized finite element method

Let $\boldsymbol{\Phi}^h := \mathbf{X}^h \times Q^h \times \Sigma^h$ be finite element subspaces of $\boldsymbol{\Phi}$ satisfying the standard approximation properties [5], i.e. for $0 \le m \le r$

$$\inf_{\mathbf{v}^h\in\mathbf{X}^h} \|\mathbf{v} - \mathbf{v}^h\|_1 \le Ch^m\|\mathbf{v}\|_{m+1} \quad \forall\, \mathbf{v} \in H^{m+1}(\Omega), \tag{23}$$

$$\inf_{\sigma^h\in\sigma^h} \|\sigma - \sigma^h\|_0 \le Ch^m\|\sigma\|_m \quad \forall\, \sigma \in H^m(\Omega), \tag{24}$$

$$\inf_{q^h\in Q^h} \|q - q^h\|_0 \le Ch^m\|q\|_m \quad \forall\, q \in H^m(\Omega). \tag{25}$$

The Galerkin finite element (GFE) method of (13)–(14) is to find $\boldsymbol{U}^h \in \mathbf{X}^h \times Q^h \times \Sigma^h$ such that

$$\mathcal{B}(\boldsymbol{U}^h, \boldsymbol{V}^h) = \mathcal{F}(\boldsymbol{V}^h) \quad \forall\, \boldsymbol{V}^h \in \boldsymbol{\Phi}^h, \tag{26}$$

where

$$\begin{aligned}
\mathcal{B}(\boldsymbol{U}^h, \boldsymbol{V}^h) &= a\left(\mu\omega^h, \nabla\times\mathbf{v}^h\right) + (1-a)\left(2\mu D(\mathbf{u}^h), D(\mathbf{v}^h)\right) - \left(p^h, \nabla\cdot\mathbf{v}^h\right)\\
&\quad + \epsilon\left(\mathbf{u}^h, \mathbf{v}^h\right) + \left(\omega^h - \nabla\times\mathbf{u}^h, \sigma^h\right) + \left(\rho\nabla\cdot\mathbf{u}^{\mathrm{h}}, q^h\right),\\
\mathcal{F}(\boldsymbol{V}^h) &= \left(\mathbf{f}, \mathbf{v}^h\right).
\end{aligned}$$

Proper selection of spaces $\mathbf{X}^h$, Q^h and Σ^h is essential to satisfy the compatibility conditions required by the inf-sup condition for the stability of finite element methods. For example, the Taylor-Hood

element uses piecewise quadratic velocity and piecewise linear pressure, a well-established and stable choice for such simulations [11,22].

We utilize equal-order polynomials as a finite element method to approximate equation (26). Among the equal-order finite element methods, we adopt the reduced Galerkin least-squares (GLS) method [4,7]. Unlike the standard GLS method, this reduced method is obtained by including only essential terms for stability, which involves a stability parameter. Additionally, certain terms with second derivatives in the second slot can be omitted when employing linear basis functions. The GLS method is implemented by introducing stability parameters α and stabilization terms B_{DS} and F_{DS} into the weak form of the governing Equation (26):

$$\mathcal{B}(\boldsymbol{U}^h, \boldsymbol{V}^h) + \alpha B_{DS}(\boldsymbol{U}^h, \boldsymbol{V}^h) = \mathcal{F}(\boldsymbol{V}^h) + \alpha F_{DS}(\boldsymbol{V}^h) \quad \forall\, \boldsymbol{V}^h \in \boldsymbol{\Phi}^h, \tag{27}$$

where

$$B_{DS}(\boldsymbol{U}^h, \boldsymbol{V}^h) = \sum_{T\in\mathcal{T}_h} \frac{h^2}{\mu}\left(a\mu\nabla\times\omega^h + \nabla p^h + (1-a)2\mu\nabla\cdot D(\mathbf{u}^h) + \epsilon\mathbf{u}^h : \nabla q^h\right), \tag{28}$$

$$F_{DS}(\boldsymbol{V}^h) = \sum_{T\in\mathcal{T}_h} \frac{h^2}{\mu}\left(\mathbf{f} : \nabla q^h\right). \tag{29}$$

Suppose $\boldsymbol{U} = (\mathbf{u}, \boldsymbol{\omega}, p) \in \mathbf{H}^{m+1}(\Omega) \times H^m(\Omega) \times H^m(\Omega)$ is a solution of (4)–(6). It is obvious that the exact solution $\boldsymbol{U}$ satisfies

$$\mathcal{B}(\boldsymbol{U}, \boldsymbol{V}^h) + \alpha B_{DS}(\boldsymbol{U}, \boldsymbol{V}^h) = \mathcal{F}(\boldsymbol{V}^h) + \alpha F_{DS}(\boldsymbol{V}^h)\ \forall \boldsymbol{V}^h \in \boldsymbol{\Phi}^h. \tag{30}$$

We establish an a priori error estimate for the solution of (27) in the following theorem

Theorem 4.1: *Suppose* $\boldsymbol{U} = (\mathbf{u}, \boldsymbol{\omega}, p) \in \mathbf{H}^{m+1}(\Omega) \times H^m(\Omega) \times H^m(\Omega)$ *is a solution of* (4)–(6). *If* $\boldsymbol{U}^h = (\mathbf{u}^h, \boldsymbol{\omega}^h, p^h) \in \boldsymbol{\Phi}^h$ *is a solution of the Galerkin least squares scheme* (27) *for sufficiently small* α *and* h, *it satisfies the estimate*

$$\|\mathbf{u} - \mathbf{u}^h\|_1 + \|p - p^h\|_0 + \|\omega - \omega^h\|_0 \le Ch^m. \tag{31}$$

Proof: Let $\tilde{\mathbf{U}}^h = (\tilde{\mathbf{u}}^h, \tilde{\boldsymbol{\omega}}^h, \tilde{p}^h) \in \boldsymbol{\Phi}^h$ be the interpolants of $\mathbf{U} = (\mathbf{u}, \boldsymbol{\omega}, p)$ satisfying the standard results (23)–(25). First, subtract (30) from (27), and add and subtract $\tilde{\mathbf{U}}^h$ in the resulting equation to get

$$\mathcal{B}(\mathbf{U}^h - \tilde{\mathbf{U}}^h, \mathbf{V}^h) + \alpha B_{DS}(\mathbf{U}^h - \tilde{\mathbf{U}}^h, \mathbf{V}^h) = \mathcal{B}(\mathbf{U} - \tilde{\mathbf{U}}^h, \mathbf{V}^h) + \alpha B_{DS}(\mathbf{U} - \tilde{\mathbf{U}}^h, \mathbf{V}^h). \tag{32}$$

Letting $\mathbf{V}^h = \mathbf{U}^h - \tilde{\mathbf{U}}^h$ in (32), we consier the lower bound of the B_{DS} term in the left side. Using Cauchy–Schwarz, Young's inequalities,

$$\begin{aligned} &B_{DS}(\mathbf{U}^h - \tilde{\mathbf{U}}^h, \mathbf{U}^h - \tilde{\mathbf{U}}^h) \\ &\ge \sum_{T\in\mathcal{T}^h} \frac{h^2}{\mu}\Big[-a\mu\|\nabla\times(\boldsymbol{\omega}^h - \tilde{\boldsymbol{\omega}}^h)\|_0\|\nabla(p^h - \tilde{p}^h))\|_0 + \|\nabla(p^h - \tilde{p}^h)\|_0^2 \end{aligned}$$

$$
\begin{aligned}
&-2(1-a)\mu\|\nabla\cdot D(\mathbf{u}^h-\tilde{\mathbf{u}}^h)\|_0\|\nabla(p^h-\tilde{p}^h))\|_0-\epsilon\|\mathbf{u}^h-\tilde{\mathbf{u}}^h\|_0\|\nabla(p^h-\tilde{p}^h))\|_0\Big]\\
&\geq\sum_{T\in\mathcal{T}^h}h^2\Big[-a^2\frac{1}{4\delta_1}\|\nabla\times(\boldsymbol{\omega}^h-\tilde{\boldsymbol{\omega}}^h)\|_0^2-\delta_1\|\nabla(p^h-\tilde{p}^h))\|_0^2+\frac{1}{\mu}\|\nabla(p^h-\tilde{p}^h)\|_0^2\\
&-(1-a)^2\frac{1}{\delta_2}\|\nabla\cdot D(\mathbf{u}^h-\tilde{\mathbf{u}}^h)\|_0^2-\delta_2\|\nabla(p^h-\tilde{p}^h)\|_0^2-\frac{\epsilon}{\mu}\frac{1}{4\delta_3}\|\mathbf{u}^h-\tilde{\mathbf{u}}^h\|_0^2\\
&-\frac{\epsilon}{\mu}\delta_3\|\nabla(p^h-\tilde{p}^h)\|_0^2\Big]\\
&\geq\sum_{T\in\mathcal{T}^h}h^2\left(\frac{1}{\mu}-\delta_1-\delta_2-\frac{\epsilon}{\mu}\delta_3\right)\|\nabla(p^h-\tilde{p}^h))\|_0^2-a^2\frac{1}{4\delta_1}C_I\|\boldsymbol{\omega}^h-\tilde{\boldsymbol{\omega}}^h\|_0^2\\
&-(1-a)^2\frac{1}{\delta_2}C_I\|D(\mathbf{u}^h-\tilde{\mathbf{u}}^h)\|_0^2-\frac{\epsilon}{\mu}\frac{1}{4\delta_3}h^2\|\mathbf{u}^h-\tilde{\mathbf{u}}^h\|_0^2,
\end{aligned}
\tag{33}
$$

where δ_i for $i=1,2,3$ are positive constants and the inverse inequality [5], $\|\nabla\times\boldsymbol{\sigma}^h\|_0\leq C_Ih^{-1}\|\boldsymbol{\sigma}^h\|_0$, was used for the last inequality in (33). Therefore, using (16) and (33)

$$
\begin{aligned}
&\mathcal{B}(\mathbf{U}^h-\tilde{\mathbf{U}}^h,\mathbf{U}^h-\tilde{\mathbf{U}}^h)+\alpha B_{DS}(\mathbf{U}^h-\tilde{\mathbf{U}}^h,\mathbf{U}^h-\tilde{\mathbf{U}}^h)\\
&\geq(1-a)\left(2\mu-\alpha(1-a)\frac{C_I}{\delta_2}\right)\|D(\mathbf{u}^h-\tilde{\mathbf{u}}^h)\|_0^2+\epsilon\left(1-\frac{\alpha h^2}{4\mu\delta_3}\right)\|\mathbf{u}^h-\tilde{\mathbf{u}}^h\|_0^2\\
&\quad+a\left(\mu-\alpha\frac{aC_I}{4\delta_1}\right)\|\boldsymbol{\omega}^h-\tilde{\boldsymbol{\omega}}^h\|_0^2+\alpha h^2\left(\frac{1}{\mu}-\delta_1-\delta_2-\frac{\epsilon}{\mu}\delta_3\right)\|\nabla(p^h-\tilde{p}^h))\|_0^2.
\end{aligned}
\tag{34}
$$

On the other hand, by (17), Young's ineqaulity and (23)–(25),

$$
\begin{aligned}
&\mathcal{B}(\mathbf{U}-\tilde{\mathbf{U}}^h,\mathbf{U}^h-\tilde{\mathbf{U}}^h)\\
&\leq C\|\mathbf{U}-\tilde{\mathbf{U}}^h|\|\|\mathbf{U}^h-\tilde{\mathbf{U}}^h|\|\\
&\leq C(\|\mathbf{u}-\tilde{\mathbf{u}}^h\|_1+\|\boldsymbol{\omega}-\tilde{\boldsymbol{\omega}}^h\|_0+\|p-\tilde{p}^h\|_0)(\|\mathbf{u}^h-\tilde{\mathbf{u}}^h\|_1+\|p^h-\tilde{p}^h\|_0+\|\boldsymbol{\omega}^h-\tilde{\boldsymbol{\omega}}^h\|)_0)\\
&\leq Ch^{2m}+\delta_4(\|\mathbf{u}^h-\tilde{\mathbf{u}}^h\|_1^2+\|\boldsymbol{\omega}^h-\tilde{\boldsymbol{\omega}}^h\|_0^2+\|p^h-\tilde{p}^h\|_0^2),
\end{aligned}
\tag{35}
$$

for some $\delta_4>0$. Also,

$$
\begin{aligned}
&B_{DS}(\mathbf{U}-\tilde{\mathbf{U}}^h,\mathbf{U}^h-\tilde{\mathbf{U}}^h)\\
&\leq\sum_{T\in\mathcal{T}^h}\frac{h^2}{\mu}\Big(a\mu\nabla\times(\boldsymbol{\omega}-\tilde{\boldsymbol{\omega}}^h)+(1-a)2\mu\nabla\cdot D(\mathbf{u}-\tilde{\mathbf{u}}^h)+\epsilon(\mathbf{u}-\tilde{\mathbf{u}}^h)+\nabla(p-\tilde{p}^h),(p^h-\tilde{p}^h)\Big)\\
&\leq C\sum_{T\in\mathcal{T}^h}h^2\Big(\|\nabla\times(\boldsymbol{\omega}-\tilde{\boldsymbol{\omega}}^h)\|_0+\|\nabla\cdot D(\mathbf{u}-\tilde{\mathbf{u}}^h)\|_0+\|\mathbf{u}-\tilde{\mathbf{u}}^h\|_0+\|\nabla(p-\tilde{p}^h)\|_0\Big)
\end{aligned}
$$

$$
\begin{aligned}
&\times \|\nabla(p^h - \tilde{p}^h)\|_0 \\
&\leq C \sum_{T\in\mathcal{T}^h} \frac{h^4}{\delta_5} \left(\|\nabla \times (\boldsymbol{\omega} - \tilde{\boldsymbol{\omega}}^h)\|_0^2 + \|\nabla \cdot D(\mathbf{u} - \tilde{\mathbf{u}}^h)\|_0^2 + \|\mathbf{u} - \tilde{\mathbf{u}}^h\|_0^2 + \|\nabla(p - \tilde{p}^h)\|_0^2 \right) \\
&\quad + \delta_5 \sum_{T\in\mathcal{T}^h} \|\nabla(p^h - \tilde{p}^h)\|_0^2 \\
&\leq Ch^4 \left(h^{2m-2}\right) + \delta_5 \sum_{T\in\mathcal{T}^h} \|\nabla(p^h - \tilde{p}^h)\|_0^2 \\
&\leq Ch^{2m+2} + \delta_5 \|\nabla(p^h - \tilde{p}^h)\|_0^2 . \qquad (36)
\end{aligned}
$$

for some $\delta_5 > 0$. Applying the estimates (34)–(36) to the Equation (32), we obtain

$$
\begin{aligned}
&(1-a)\left(2\mu - \alpha(1-a)\frac{C_I}{\delta_2} - \delta_4 K_1\right) \|D(\mathbf{u}^h - \tilde{\mathbf{u}}^h)\|_0^2 + \epsilon\left(1 - \frac{\alpha h^2}{4\mu\delta_3}\right) \|\mathbf{u}^h - \tilde{\mathbf{u}}^h\|_0^2 \\
&\quad + a\left(\mu - \alpha\frac{aC_I}{4\delta_1} - \delta_4\right) \|\boldsymbol{\omega}^h - \tilde{\boldsymbol{\omega}}^h\|_0^2 \\
&\quad + \alpha h^2 \left(\frac{1}{\mu} - \delta_1 - \delta_2 - \frac{\epsilon}{\mu}\delta_3 - \delta_4 K_2 - \delta_5\right) \|\nabla(p^h - \tilde{p}^h)\|_0^2 \\
&\leq Ch^{2m}, \qquad (37)
\end{aligned}
$$

where we used $\|\mathbf{u}^h - \tilde{\mathbf{u}}^h\|_1 \leq M_1 \|D(\mathbf{u}^h - \tilde{\mathbf{u}}^h)\|_0$ and $\|p^h - \tilde{p}^h\|_0 \leq K_2 \|\nabla(p^h - \tilde{p}^h)\|_0$ for K_1, $K_2 > 0$. Choose sufficiently small δ_i for $i = 1, \ldots, 5$ so that the coefficient of the last term in (37) is positive. If α, h are small enough to yield positive coefficients of other terms in (37), the estimate (31) follows from the triangular inequality. ■

These terms depend on the residual of the momentum equation and thus ensure the consistency of the stabilized formulation [9]. The specific positive constant α is dependent on the details of the simulation and may need to be adjusted for optimal results [12].

4.2. LS finite element method

Let $\boldsymbol{\Phi}_1^h := \mathbf{X}^h \times Q_1^h \times \Sigma_1^h$ be finite element subspaces of $\boldsymbol{\Phi}_1$ satisfying the standard approximation properties (23)–(25). The discrete LS minimization problem for the Brinkman Equations (10)-(12) is to choose $\boldsymbol{U}^h \in \boldsymbol{\Phi}_1^h$ such that

$$
L(\boldsymbol{U}^h; \mathbf{f}) = \inf_{\boldsymbol{V}^h = (\mathbf{v}^h, \sigma^h, q^h) \in \boldsymbol{\Phi}_1^h} L(\boldsymbol{V}^h; \mathbf{f}). \qquad (38)
$$

The finite approximation to (38) is equivalent to seek to find $\boldsymbol{U}^h \in \mathbf{X}^h \times \Sigma_1^h \times Q_1^h$ such that

$$
\mathcal{B}_{LS}(\boldsymbol{U}^h, \boldsymbol{V}^h) = \mathcal{F}(\boldsymbol{V}^h) \quad \forall\, \boldsymbol{V}^h \in \mathbf{X}^h \times \Sigma_1^h \times Q_1^h, \qquad (39)
$$

where

$$\begin{aligned}\mathcal{B}_{LS}(\boldsymbol{U}^h, \boldsymbol{V}^h) = &\sum_{T\in\mathcal{T}_h}\left(\mu\nabla\times\omega^h + \nabla p^h + \epsilon\mathbf{v}^h : \mu\nabla\times\sigma^h + \nabla q^h + \epsilon\mathbf{v}^h\right)\\ &+ \sum_{T\in\mathcal{T}_h} K\left(\rho\nabla\cdot\mathbf{u}^h : \rho\nabla\cdot\mathbf{v}^h\right)\\ &+ \sum_{T\in\mathcal{T}_h}\left(\omega^h - \nabla\times\mathbf{u}^h : \sigma^h - \nabla\times\mathbf{v}^h\right),\\ \mathcal{F}(\boldsymbol{V}^h) = &\sum_{T\in\mathcal{T}_h}\left(\mathbf{f} : \mu\nabla\times\sigma^h + \nabla q^h + \epsilon\mathbf{v}^h\right).\end{aligned}$$

We establish an a priori error estimate for the solution of (39) in the following theorem

Theorem 4.2: *Let* $\boldsymbol{U} = (\mathbf{u}, \boldsymbol{\omega}, p) \in \mathbf{H}^{m+1}(\Omega) \times H^{m+1}(\Omega) \times H^{m+1}(\Omega)$ *be the velocity–pressure–vorticity formulation of Brinkman Equations* (10)–(12). *Suppose* ϵ *is sufficiently small. Then there exists a unique solution* $\boldsymbol{U}^h = (\mathbf{u}^h, \omega^h, p^h) \in \boldsymbol{\Phi}_1^h$ *satisfying LS minimization problem* (22) *such that*

$$\|\mathbf{u} - \mathbf{u}^h\|_1 + \|p - p^h\|_0 + \|\omega - \omega^h\|_0 \leq Ch^m. \tag{40}$$

Proof: The orthogonal property $\mathcal{B}_{LS}(\boldsymbol{U} - \boldsymbol{U}^h, V^h) = 0$ for all $V^h = (\mathbf{v}^h, \sigma^h, q^h) \in \boldsymbol{\Phi}_1^h$ and the bounds (20) and (21) directly leads to the bound

$$\|\mathbf{u} - \mathbf{u}^h\|_1 + \|p - p^h\|_0 + \|\omega - \omega^h\|_0 \leq \inf_{\boldsymbol{V}^h\in\boldsymbol{\Phi}^h} \frac{c_1}{c_0}\left(\|\mathbf{u} - \mathbf{v}^h\|_1^2 + \|p - q^h\|_1 + \|\omega - \sigma^h\|_1\right),$$

which, using the approximation properties in (23)–(25), yields the desired error bound. ■

5. Numerical results

In our numerical experiments, we employed the GFE in (26), the GLS in (27), and the LS in (38) methods to solve the system of Equations (1)–(3). We implemented element pairs (P_2, P_1, P_1) and (P_1, P_1, P_1) for velocity, pressure, and vorticity, respectively. We considered three variations of the GLS method in (27) and (28):

- VPD formulation: This formulation emphasizes the relationship between velocity, pressure, and the rate of deformation tensor in the momentum equation for the GLS method with $a = 0$.
- VPDW formulation: The formulation extends the GLS method with $0 < a < 1$ to include velocity, pressure, the rate of deformation tensor, and vorticity in the momentum equation, allowing for a more comprehensive analysis. Here, we considered $a = 0.5$.
- VPW formulation: The formulation further extends the GLS method with $a = 1$ by focussing on the interactions between velocity, pressure, and vorticity in the momentum equation.

In addition, we implemented the LS method as an alternative approach. The interpretation and discussion of these results will follow in the subsequent sections, shedding light on the insights gained from our numerical experiments and their implications for the broader understanding of fluid flow in porous media.

5.1. Test problem

We consider a non-physical example [3]. The parameters $\mu = 1$ and $\rho = 1$ are considered in (4)–(6). The domain Ω for the model equations is defined as $\Omega = (0, 1)^2$. The source term $\mathbf{f}$ in (4) is chosen

so that the exact solutions for the velocity $\mathbf{u}$, pressure p, and vorticity ω are

$$\mathbf{u} = \left(-2\pi\cos(2\pi x)\sin(2\pi y), 2\pi\sin(2\pi x)\cos(2\pi y)\right),$$
$$p = \sin(2\pi x)\sin(2\pi y),$$

and

$$\omega = 8\pi^2\sin(2\pi x)\sin(2\pi y),$$

respectively. Boundary conditions enforce the exact solutions on the domain boundary. To perform numerical experiments, we employ linear basis functions for all variables. The domain Ω is discretized using uniform Union Jack grids with three different grid sizes: $h = 1/32$, $1/64$, and $1/128$. Figure 1 displays the solution of the GLS method with $a = 0$ (VPD) on a uniform Union Jack grid with $h = 1/64$ at $(\kappa, \alpha) = (1, 0.005)$, demonstrating seepage velocity arrows.

In the following figures, we illustrate the convergence rates of the VPD solutions for $(\mathbf{u}, p, \omega)$. Figure 2 demonstrates convergence rates of $O(h^2)$ in the L^2-norm for $(\mathbf{u}, p, \omega)$, considering different values of κ while keeping α fixed at 0.005. In Figure 3, we present the convergence rates of the VPD solutions with various α values while maintaining κ at 1. These results highlight improvements in the accuracy of the pressure variable (p) when α is set to 0.5. The findings from the VPD method suggest that using $\alpha = 0.5$ can decrease the L^2 error in the pressure variable.

Finally, Figure 4 provides the convergence rates of four linear equal-order finite element methods for the Brinkman equations with $\epsilon = \mu/\kappa = 1$: the LS with $K = 10^3$ and the GLS methods with $\alpha = 0.005$ for various values of a (0 for VPD, 0.5 for VPDW, 1 for VPW). These results demonstrate nearly optimal convergence rates of $O(h^2)$ in the L^2-norm for all cases. Furthermore, the VPDW and VPW methods prove effective in reducing errors compared to VPD solutions, and except for velocity, the results of LS are similar to that. The most favourable performance was observed when employing the VPW method.

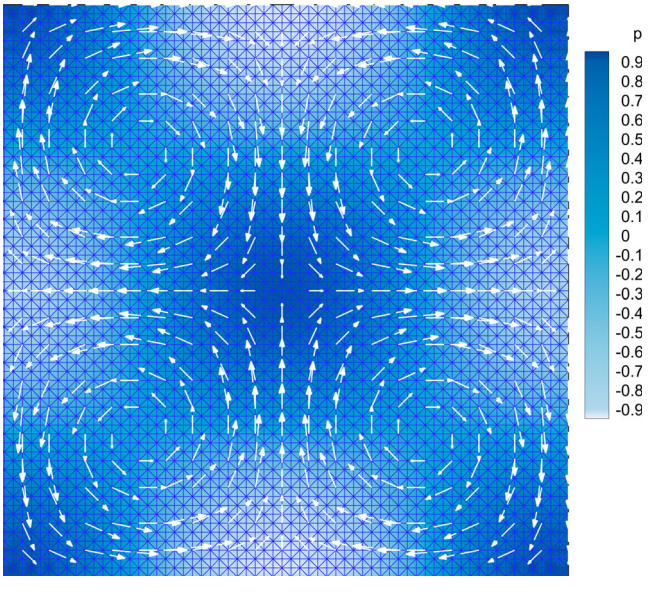

Figure 1. The seepage velocity $\mathbf{u}$ (arrows) and the pressure p (contours) at $\kappa = 1$ on uniform Union Jack grids as $h = 1/64$ using the VPD form at $\alpha = 0.005$.

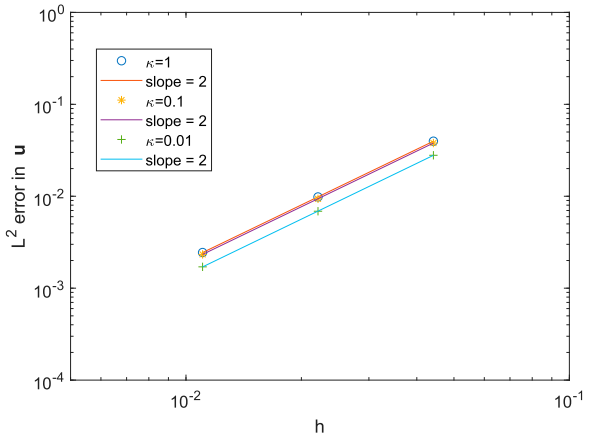

(a) $\mathbf{u}$

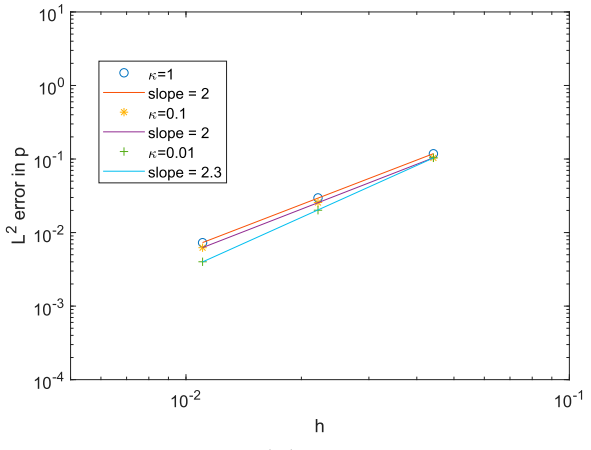

(b) p

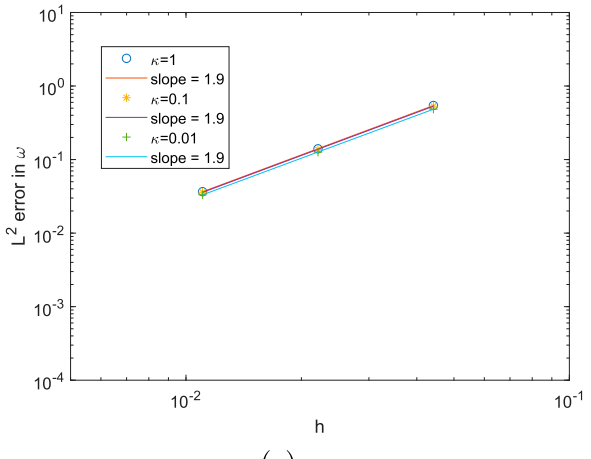

(c) ω

Figure 2. L^2 errors of (a) $\mathbf{u}$, (b) p, and (c) ω for the GLS with $a = 0$ (VPD) at $(\kappa, \alpha) = (1, 0.005)$, $(0.1, 0.005)$, and $(0.01, 0.005)$.

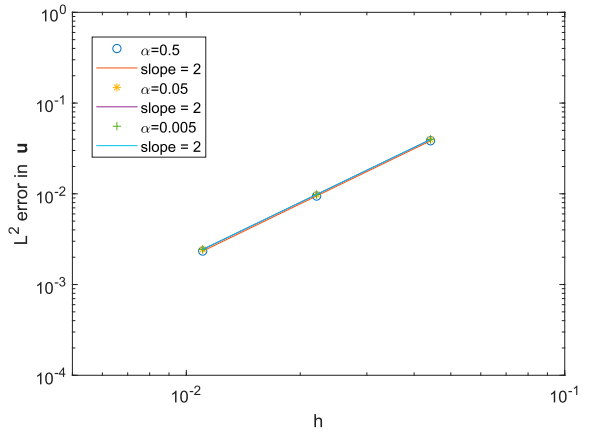

(a) $\mathbf{u}$

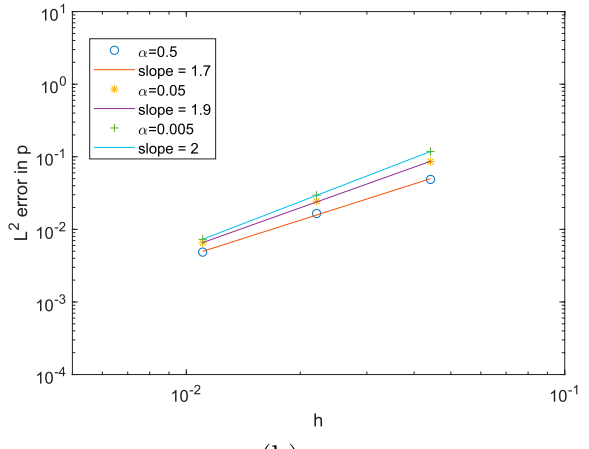

(b) p

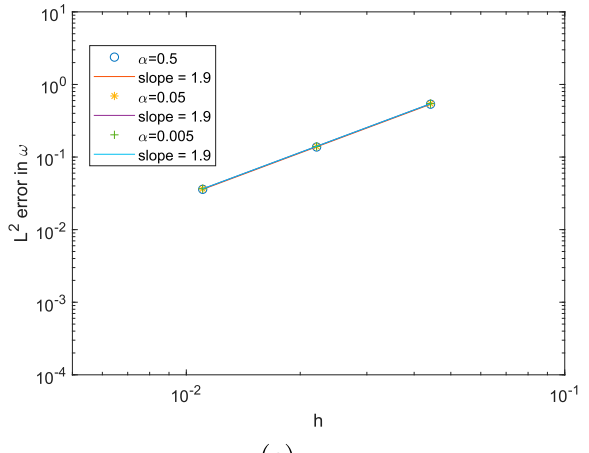

(c) ω

Figure 3. L^2 errors of (a) $\mathbf{u}$, (b) p, and (c) ω for the GLS with $a = 0$ (VPD) at $(\kappa, \alpha) = (1, 0.005)$, $(1, 0.05)$, and $(1, 0.5)$.

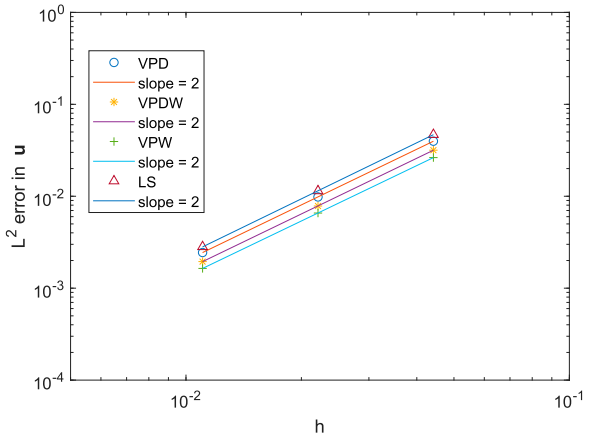

(a) $\mathbf{u}$

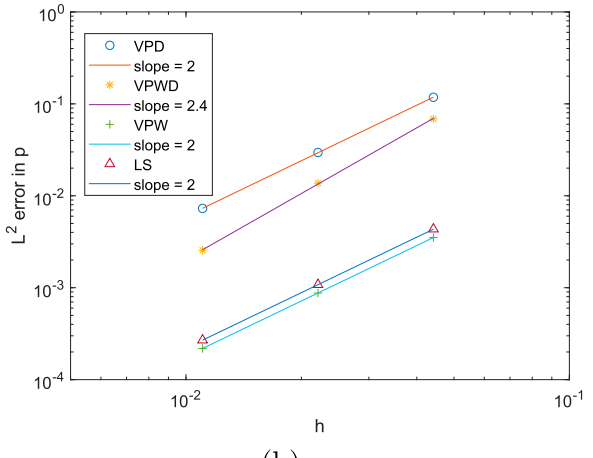

(b) p

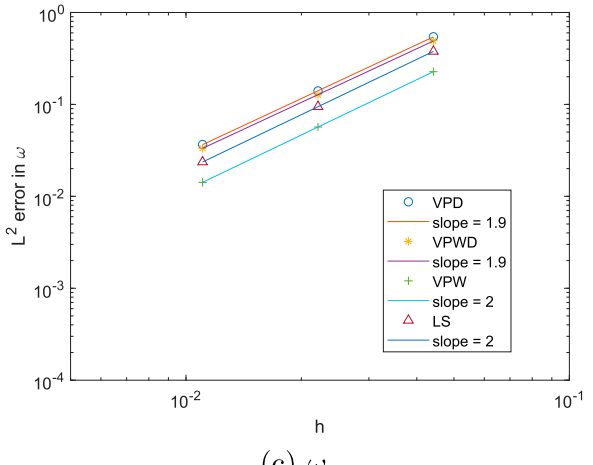

(c) ω

Figure 4. $\epsilon = 1$. L^2 errors of (a) $\mathbf{u}$, (b) p, and (c) ω for the GLS with $a = 0$ (VPD), 0.5 (VPDW), and 1 (VPW) and the LS with $K = 10^3$.

5.2. Pore-Scale flow problem

In this study, we utilize one of the SEM images from Keller, Auset, and Sirivithayapakorn's pore-scale flow experiments to determine flow velocity and pressure drop in the pore throats [2,26]. The model focuses exclusively on the pore space, as depicted in Figure 5, with the solid regions excluded. The spatial area considered is 640 μm by 320 μm, and it simulates the flow of water from right to left across the geometry. The inlet and outlet fluid pressures are known, and it is further assumed there are the top and bottom symmetric boundaries. Importantly, the flow within the pores is assumed to not penetrate the solid grains.

The boundary domain Γ is defined as $\Gamma = \Gamma_{\text{in}} \cup \Gamma_{\text{w}} \cup \Gamma_{\text{out}} \cup \Gamma_{\text{s}}$, where Γ_{in}, Γ_{w}, Γ_{out}, and Γ_{s} are the inlet, wall, outlet, and symmetric boundaries, respectively. To simplify the finite element formulation and its presentation, we assumed the homogeneous boundary conditions on Γ for $\mathbf{u}$. On the boundaries along the wall Γ_{w}, $\mathbf{u} = \mathbf{0}$. On the axis of symmetry Γ_{s}, we assume standard symmetric boundary conditions $\mathbf{u} \cdot \mathbf{n} = 0$, where $\mathbf{n}$ is outward unit normal vectors. Problems with nonhomogeneous boundary conditions on Γ_{in} and Γ_{out} will be considered for numerical tests of creeping flow, which can be formulated analogously.

We employed the GFE, the GLS with $\alpha = 0.5$, and the LS with $K = 10^3$ methods to tackle pore-scale flow problems, which were previously investigated [2,26]. We used the parameters μ, ρ, and κ (Table 1) to characterize the fluid rheology [8].

Our initial investigation focussed on the Brinkman equations in (1) with $\epsilon = 0$, essentially corresponding to the Stokes equations. For our numerical tests, we considered the Stokes equations with nonhomogeneous boundary conditions on Γ_{in} ($p = p_i$) and Γ_{out} ($p = p_o$), as depicted in Figure 5. The Stokes system was discretized using elements (P_2, P_1, P_1) and (P_1, P_1, P_1) for $(\mathbf{u}, p, \omega)$, resulting in a degree of freedom (DOF) of 452566 and 185640, respectively.

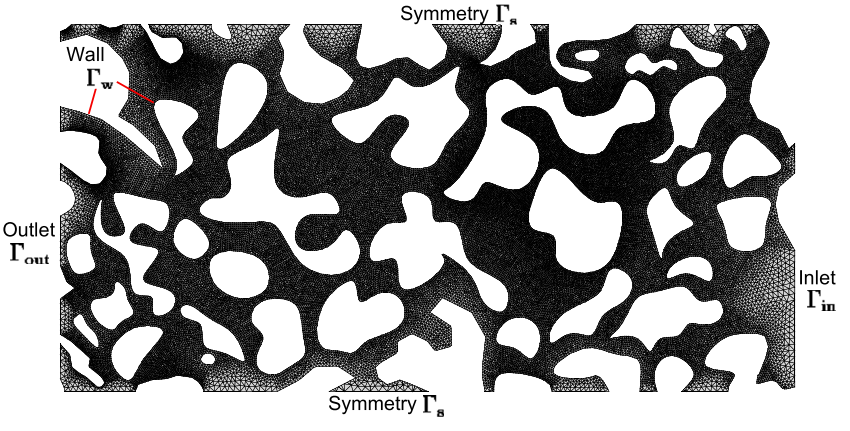

Figure 5. A 640 μm by 320 μm geometry and boundary conditions and finite element mesh.

Table 1. Symbols and values of physical and numerical constants and parameters used in pore-scale flow problem.

Parameter	Symbol	Value	Units
Fluid density	ρ	1000	kg/m^3
Fluid viscosity	μ	0.001	kg/(m · s)
Pressure on the inlet	p_i	0.715	pa
Pressure on the outlet	p_o	0	pa
Permeability	κ	9.86922×10^{-13}	m^2
Velocity on the inlet	u_i	$-10^{-4} \sim -10^{-5}$	m/s

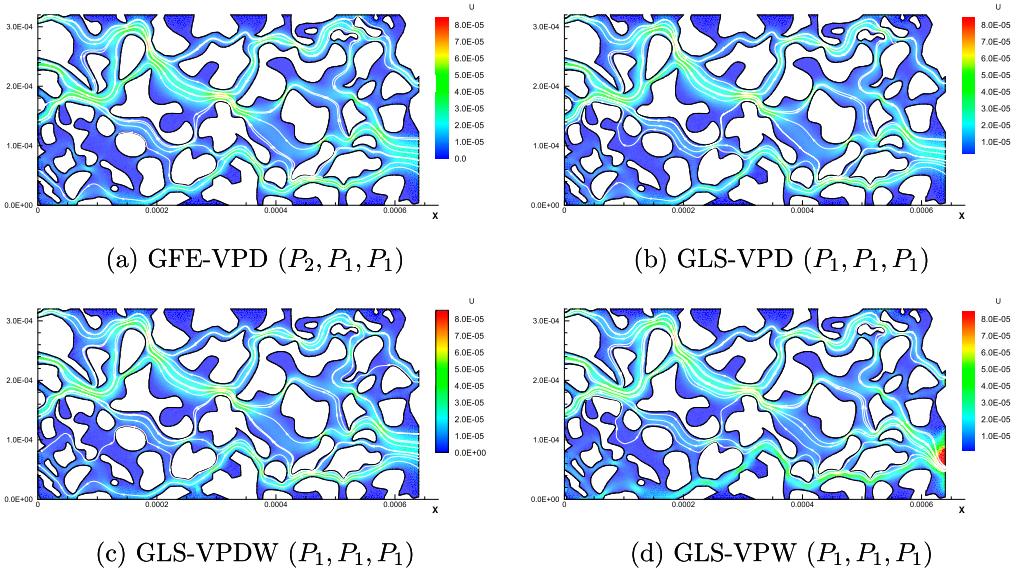

Figure 6. Stokes equations. The magnitude of velocity contours, streamline of the (a) GFE with $a = 0$ (VPD) at $(\mathbf{u}, p, \omega, DOF) = (P_2, P_1, P_1, 452566)$, GLS with (b) $a = 0$ (VPD), (c) $a = 0.5$ for VPDW, and (d) $a = 1$ (VPW) at $(\mathbf{u}, p, \omega, DOF) = (P_1, P_1, P_1, 185640)$.

To illustrate the impact of the choice of diffusion stabilization terms, we present the magnitude of velocity contours for the GFE and the GLS methods with different values of a (0 for VPD, 0.5 for VPDW, and 1 for VPW) applied to the Stokes equations in Figure 6. The results in Figure 6 demonstrate that for elements $(\mathbf{u}, p, \omega) = (P_2, P_1, P_1)$, the GFE method produces smooth velocity and pressure contours, similar to those obtained with the GLS-VPD and GLS-VPDW methods for elements $(\mathbf{u}, p, \omega) = (P_1, P_1, P_1)$. These velocity contours for the Stokes flows match the results obtained from Comsol software [8]. However, the GLS-VPW method exhibits unstable velocity values near the inlet (Figure 6(d)). These findings suggest that employing the GLS-VPD and GLS-VPDW methods for the Stokes equations can lead to a reduction in the degree of freedom (DOF) from 452566 to 185640 while including the stabilization terms for the VPD and VPDW methods proves valuable for accurately capturing velocity profiles. Furthermore, the rate of deformation tensor D has a stabilizing effect on the velocity.

In Figure 7, we applied the GFE methods to approximate the Brinkman system, varying the values of a (0 for VPD, 0.5 for VPDW, and 1 for VPW). The results depicted in Figure 7 illustrate that, for elements $(\mathbf{u}, p, \omega) = (P_2, P_1, P_1)$, the GFE-VPD method produces smooth velocity and pressure contours. When employing elements $(\mathbf{u}, p, \omega) = (P_1, P_1, P_1)$ for all three GFE methods, only GFE-VPDW exhibits velocity contours consistent with those of the GFE-VPD method with elements $(\mathbf{u}, p, \omega) = (P_2, P_1, P_1)$ (Figure 7(a)). In the following Figure 8, we provide velocity, streamline, and pressure contours obtained using the LS method with $K = 10^3$ and the GLS methods with different values of a (0 for VPD, 0.5 for VPDW, and 1 for VPW). These results are obtained with $(\mathbf{u}, p, \omega) = (P_1, P_1, P_1)$ elements. The observations in Figure 8 indicate that the three methods yield similar pressure contours. These results show that the stabilization term B_{SD} stabilizes velocity and pressure contours. Our findings demonstrate the effectiveness of the stabilized GLS methods for the Brinkman equations, reducing the degrees of freedom from 452566 to 185640 while maintaining comparable accuracy.

Furthermore, in Figure 8, while the three GLS methods consistently exhibit both the magnitude of velocity and pressure contours, the LS method lacks velocity contours. This discrepancy can be

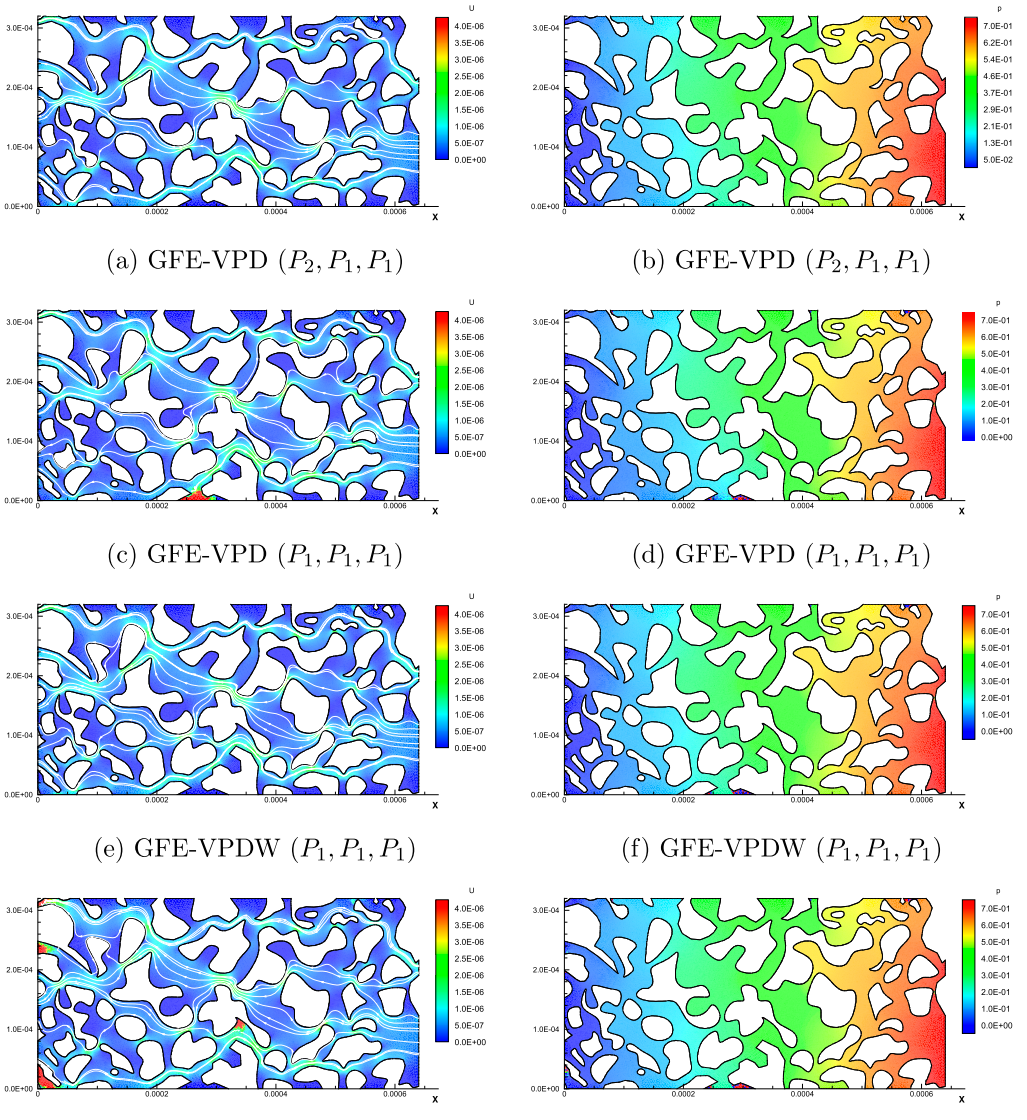

(a) GFE-VPD (P_2, P_1, P_1) (b) GFE-VPD (P_2, P_1, P_1)

(c) GFE-VPD (P_1, P_1, P_1) (d) GFE-VPD (P_1, P_1, P_1)

(e) GFE-VPDW (P_1, P_1, P_1) (f) GFE-VPDW (P_1, P_1, P_1)

(g) GFE-VPW (P_1, P_1, P_1) (h) GFE-VPW (P_1, P_1, P_1)

Figure 7. Brinkman equations. The magnitude of velocity contours, streamline, pressure contours of the GFE with $a = 0$ (VPD) at $(\mathbf{u}, p, \omega, DOF) = (P_2, P_1, P_1, 452566)$ and the GFE with $a = 0$ (VPD), $a = 0.5$ (VPDW), and $a = 1$ (VPW) at $(\mathbf{u}, p, \omega, DOF) = (P_1, P_1, P_1, 185640)$. (a) GFE-VPD (P_2, P_1, P_1) (b) GFE-VPD (P_2, P_1, P_1) (c) GFE-VPD (P_1, P_1, P_1) (d) GFE-VPD (P_1, P_1, P_1) (e) GFE-VPDW (P_1, P_1, P_1) (f) GFE-VPDW (P_1, P_1, P_1) (g) GFE-VPW (P_1, P_1, P_1) (h) GFE-VPW (P_1, P_1, P_1).

attributed to the fact that, in the LS method, we establish the coerciveness of $L(\boldsymbol{U}; \mathbf{0})$ in (20) for sufficiently small ϵ. However, as shown in Table 1, the LS method encounters a challenge due to a significantly large $\epsilon = \mu/\kappa > 10^{10}$ at a low $\kappa = 10^{-13}$, which might fail to satisfy the coerciveness condition of $L(\boldsymbol{U}; \mathbf{0})$. Therefore, the GLS method is more suitable for the Brinkman equation at a low permeability than the LS method.

We next extended our examination to encompass the Stokes and Brinkman problems. For these numerical tests, we applied nonhomogeneous boundary conditions on Γ_{in} $(\mathbf{u} = (u_i, 0))$, and Γ_{out} $(p = p_o)$. Figure 9 shows the pressure contours for the Stokes and Brinkman problems. These contours

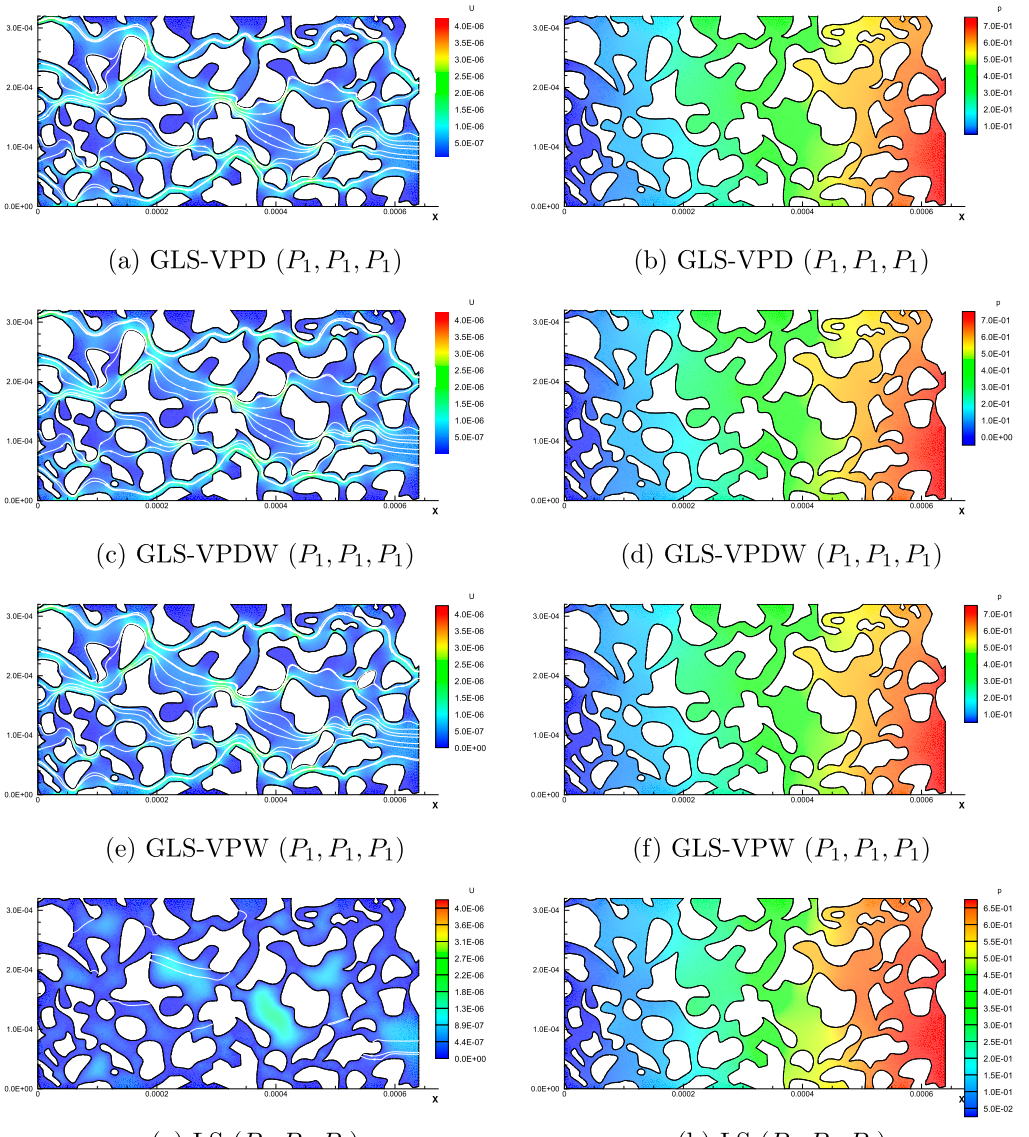

(a) GLS-VPD (P_1, P_1, P_1) (b) GLS-VPD (P_1, P_1, P_1)

(c) GLS-VPDW (P_1, P_1, P_1) (d) GLS-VPDW (P_1, P_1, P_1)

(e) GLS-VPW (P_1, P_1, P_1) (f) GLS-VPW (P_1, P_1, P_1)

(g) LS (P_1, P_1, P_1) (h) LS (P_1, P_1, P_1)

Figure 8. Brinkman equations. The magnitude of velocity contours, streamline, and pressure contours of the GLS with $a = 0$ (VPD), $a = 0.5$ (VPDW), $a = 1$ (VPW) and the LS with $K = 10^3$ at $(\mathbf{u}, p, \omega, DOF) = (P_1, P_1, P_1, 185640)$. (a) GLS-VPD (P_1, P_1, P_1) (b) GLS-VPD (P_1, P_1, P_1) (c) GLS-VPDW (P_1, P_1, P_1) (d) GLS-VPDW (P_1, P_1, P_1) (e) GLS-VPW (P_1, P_1, P_1) (f) GLS-VPW (P_1, P_1, P_1) (g) LS (P_1, P_1, P_1) (h) LS (P_1, P_1, P_1).

were derived using the GLS-VPD method. We calculated the average pressure difference d to quantify and compare the results. The formula used to define d is presented below:

$$d = \Sigma_{k=1}^{n} \frac{d_k}{n}, \tag{41}$$

where $d_k = p_{i,k} - p_{o,k}$ at x_k, $k = 1, 2, \ldots, n$. This calculation is performed for the Stokes and Brinkman equations, considering various magnitudes of velocity $U = |\mathbf{u}|$ at the inlet in the range

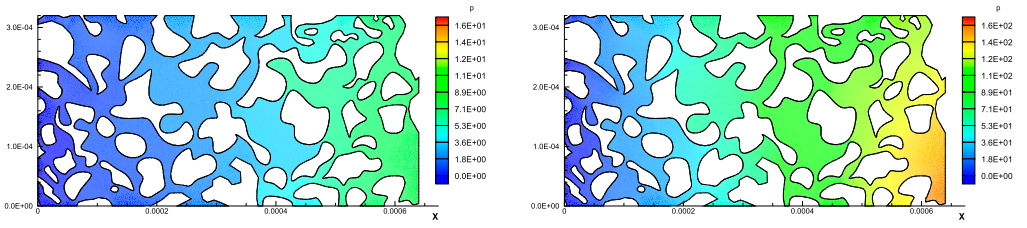

(a) Stokes equations (b) Brinkman equations

Figure 9. Pressure contours of the GLS-VPD method at $(\mathbf{u}, p, DOF, u_i) = (P_1, P_1, 185640, -10^{-4})$ for the (a) Stokes and (b) Brinkman equations.

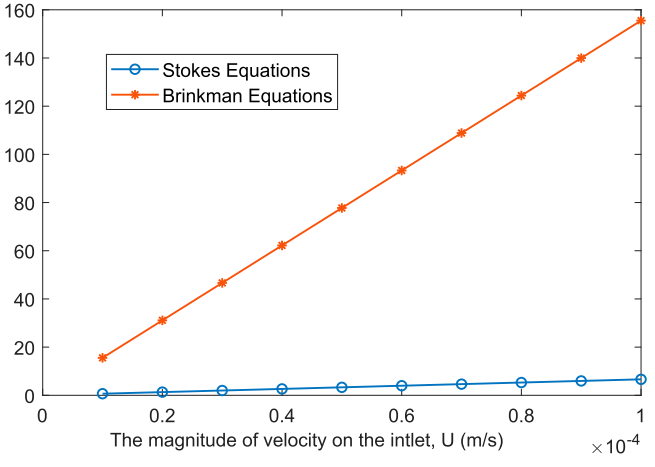

Figure 10. The average pressure difference d of the Stokes and Brinkman equations for various magnitudes of velocity U on the inlet between 10^{-5} and 10^{-4} at $p_o = 0$.

between 10^{-5} and 10^{-4}, with $p_o = 0$. As shown in Figure 10, the results clearly demonstrate a significant increase in the average pressure difference for the Brinkman equations compared to the Stokes equations as the inlet velocity U increases. The results highlight the use of the Brinkman equation to capture a noticeable amplification in the average pressure difference as the inlet velocity increases. This observation suggests that the Brinkman simulation is more realistic and accurate than the Stokes simulation in the effects of the porous medium on the flow.

6. Conclusion

In this study, we have developed linear equal-order finite element techniques for the mixed formulation of the Brinkman problem. We explored three distinct GLS methods: VPD, VPW, and VPDW, each enhanced with stabilization terms. Additionally, we applied a LS approach made by L^2 residuals of equations. Our analysis encompassed critical properties such as coercivity and continuity and provided error estimates.

We commenced our investigation with a non-physical illustrative case, employing numerical experiments to affirm the validity of our theoretical findings. These experiments exemplified impressive convergence rates of these methods, demonstrating error reduction at an optimal $O(h^2)$ rate in the L^2 norm. Using the GLS-VPDW and GLS-VPW methods effectively mitigated errors compared

to the GLS-VPD. Particularly noteworthy was the remarkable error reduction achieved with the GLS-VPW method. Furthermore, we extended the application of these methods to address a benchmark problem aimed at simulating pore-scale flow dynamics. In this practical application, the solutions obtained using the GLS-VPD and GLS-VPDW methods closely aligned with previously published work, underscoring the reliability of our approach, showing the rate of deformation tensor is included to produce a stable effect on the solution. The GLS method can be used for the Brinkman equation at a low permeability compared to the LS method. A mixed GLS method also promises to reduce the elements required for accurate simulations, making it a compelling avenue for future research.

Furthermore, our research has revealed a significant increase in the average pressure difference in the Brinkman problem compared to the Stokes equation as the inlet velocity increases. This observation provides valuable insights into the unique behaviour of Brinkman equations within porous media, enhancing our understanding of fluid flow in such environments.

The differences in results between the two models underscore the critical importance of selecting the appropriate model for simulating the given scenario. The Stokes equations, not necessitating the specification of the permeability parameter, are advantageous for scenarios where the effects of the porous structure are negligible. On the other hand, the Brinkman equations, incorporating the impact of permeability in porous media, become essential when modelling flows through mediums with significant permeability.

Disclosure statement

No potential conflict of interest was reported by the author(s).

Funding

The first author gratefully acknowledges the financial support provided in part by the National Science and Technology Council of Taiwan under grant 112-2115-M-160-001. The second author is grateful for the financial support provided in part by the US National Science Foundation under grant DMS-2207971.

References

[1] V. Anaya, D. Mora, R. Oyarzúa, and R. Ruiz-Baier, *A priori and a posteriori error analysis of a mixed scheme for the Brinkman problem*, Numer. Math. 133 (2016), pp. 781–817.
[2] M. Auset and A.A. Keller, *Pore-scale processes that control dispersion of colloids in saturated porous media*, Water Resour. Res. 40 (2004), p. W03503.
[3] S. Badia and R. Condina, *Unified stabilized finite element formulations for the Stokes and the Darcy problems*, SIAM J. Numer. Anal. 47 (2009), pp. 1971–2000.
[4] J. Bonvin, M. Picasso, and R. Stenberg, *GLS and EVSS methods for a three-field Stokes problem arising from viscoelastic flows*, Comput. Methods Appl. Mech. Eng. 190 (2001), pp. 3893–3914.
[5] S. Brenner and L. Scott, *The Mathematical Theory of Finite Element Methods*, Springer-Verlag, New York, 1994.
[6] C.L. Chang and S.Y. Yang, *Analysis of the L^2 least-squares finite element method for the velocity–vorticity–pressure Stokes equations with velocity boundary conditions*, Appl. Math. Comput.130 (2002), pp. 121–144.
[7] T.F. Chen, H. Lee, and C.C. Liu, *A study on the Galerkin least-squares method for the Oldroyd-B model*, Comput. Methods Appl. Math. 60 (2018), pp. 1024–1040.
[8] C. Comsol Inc., Pore-scale flow: Created in COMSOL Multiphysics 6.1.
[9] J. Donea and A. Huerta, *Finite Element Methods for Flow Problems*, John Wiley Sons, England, 2003.
[10] R. Guenette and M. Fortin, *A new mixed finite element method for computing viscoelastic flows*, J. Non-Newton. Fluid Mech. 60 (1995), pp. 27–52.
[11] C. Helanow and J. Ahlkrona, *Stabilized equal low-order finite elements in ice sheet modeling accuracy and robustness*, Comput. Geosci. 22 (2018), pp. 951–974.
[12] T.J.R. Hughes, L.P. Franca, and M. Balestra, *A new finite element formulation for computational fluid dynamics: V. Circumventing the Babŭska-Brezzi condition: a stable Petrov-Galerkin formulation of the stokes problem accommodating equal-order interpolation*, Comp. Meth. Appl. Mech. Eng. 59 (1986), pp. 85–99.
[13] W.R. Hwang and S.G. Advani, *Numerical simulations of Stokes-Brinkman equations for permeability prediction of dual scale fibrous porous media*, Phys. Fluids 22 (2010), p. 113101.
[14] O. Iliev, Z. Lakdawala, and V. Starikovicius, *On a numerical subgrid upscaling algorithm for Stokes-Brinkman equations*, Comput. Math. Appl. 65 (2013), pp. 435–448.

[15] P. Ingeram, *Finite element approximation of nonsolenoidal, viscous flows around porous and solid obstacles*, SIAM J. Numer. Anal. 49 (2017), pp. 491–520.
[16] H.C. Lee, *A nonlinear weighted least-squares finite element method for the Oldroyd-B viscoelastic flow*, Appl. Math. Comput. 219 (2012), pp. 421–434.
[17] H.C. Lee, *Weighted least-squares finite element methods for the linearized Navier–Stokes equations*, Int. J. Comput. Math. 91 (2014), pp. 1964–1985.
[18] H.C. Lee, *Adaptive weights for mass conservation in a least-squares finite element method*, Int. J. Comput. Math. 95 (2018), pp. 20–35.
[19] H.C. Lee, *A least-squares finite element method for steady flows across an unconfined square cylinder placed symmetrically in a plane channel*, J. Math. Anal. Appl. 504 (2021), p. 125426.
[20] H.C. Lee and H. Lee, *Equal lower-order finite elements of least-squares type in Biot poroelasticity modeling*, Taiwan. J. Math. 27 (2023), pp. 971–988.
[21] H. Leng and H. Chen, *Adaptive HDG methods for the Brinkman equations with application to optimal control*, J. Sci. Comput. 87 (2021), p. 46.
[22] W. Leng, J. Lili, Y. Xie, T. Cui, and M. Gunzburger, *Finite element three-dimensional Stokes ice sheet dynamics model with enhanced local mass conservation*, J. Comput. Phys. 274 (2014), pp. 299–311.
[23] H. Liu, P.R. Patil, and U. Narusawa, *On Darcy-Brinkman equation: viscous flow between two parallel plates packed with regular square arrays of cylinders*, Entropy 9 (2007), pp. 118–131.
[24] J. Liu, Y. Wang, and R. Song, *A Pore Scale Flow Simulation of Reconstructed Model Based on the Micro Seepage Experiment, Geofluids 2017* (2017), p. 7459346.
[25] L. Mu, *A uniformly robust H(div) weak galerkin finite element methods for Brinkman problems*, SIAM J. Sci. Numer. Anal. 58 (2020), pp. 1422–1439.
[26] S. Sirivithayapakorn and A.A. Keller, *Transport of colloids in saturated porous media: A pore-scale pbservation of the size exclusion effect and colloid acceleration*, Water Resour. Res. 39 (2003), p. 1109.
[27] P.S. Vassilevski and U. Villa, *A mixed formulation for the Brinkman problem*, SIAM J. Sci. Numer. Anal. 52 (2014), pp. 258–281.
[28] X. Wang, X. Ye, S. Zhang, and P. Zhu, *A weak Galerkin least squares finite element method of Cauchy problem for Poisson equation*, J. Compt. Appl. Math. 401 (2021), p. 113767.
[29] X. Zhang and M. Feng, *A projection-based stabilized virtual element method for the unsteady incompressible Brinkman equations*, Appl. Math. Comput. 408 (2021), p. 126325.